Chemical Engineering Science 257 (2022) 117703

Contents lists available at ScienceDirect

Chemical Engineering Science

journal homepage: www.elsevier.com/locate/ces

Effects of gravity modulation on the dynamics of a radial $A + B \rightarrow C$ reaction front

Yorgos Stergiou [a,b,*], Marcus J.B. Hauser [c], Alessandro Comolli [d], Fabian Brau [d], Anne De Wit [d], Gábor Schuszter [e], Paszkál Papp [e], Dezső Horváth [f], Clément Roux [g], Véronique Pimienta [g], Kerstin Eckert [a,b], Karin Schwarzenberger [a,b]

[a] Institute of Fluid Dynamics, Helmholtz-Zentrum Dresden-Rossendorf, Bautzner Landstr. 400, 01328 Dresden, Germany
[b] Institute of Process Engineering and Environmental Technology, Technische Universität Dresden, 01062 Dresden, Germany
[c] Faculty of Natural Science, Otto-von-Guericke-Universität Magdeburg, Universitätsplatz 2, 39106 Magdeburg, Germany
[d] Nonlinear Physical Chemistry Unit, Service de Chimie Physique et Biologie Théorique, Faculté des Sciences, Université Libre de Bruxelles (ULB), CP 231, 1050 Brussels, Belgium
[e] Department of Physical Chemistry and Materials Science, University of Szeged, Rerrich Béla tér 1., Szeged, Hungary
[f] Department of Applied and Environmental Chemistry, University of Szeged, Rerrich Béla tér 1., Szeged, Hungary
[g] Laboratoire des IMRCP, Université de Toulouse, CNRS UMR 5623, Université Toulouse III - Paul Sabatier, France

HIGHLIGHTS

- Radial $A + B \rightarrow C$ reaction fronts are investigated under modulated gravity
- Gravity modulation affects radial reaction front dynamics in Hele-Shaw cells
- Production rate is increased in fronts subject to a modulated gravity environment
- Production rate is decreased under pure microgravity conditions

GRAPHICAL ABSTRACT

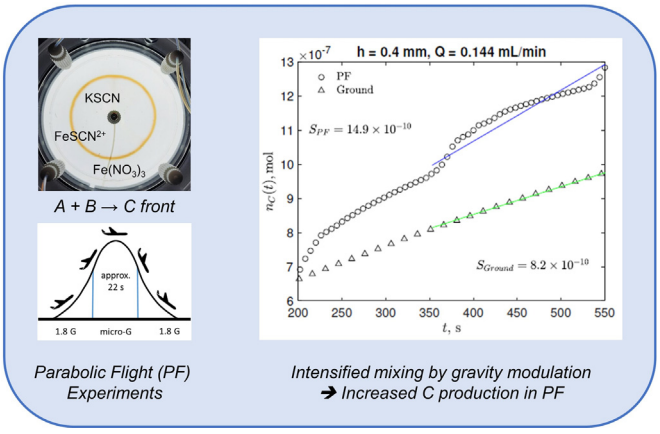

ARTICLE INFO

Article history:
Received 9 February 2022
Received in revised form 21 April 2022
Accepted 25 April 2022
Available online 30 April 2022

Keywords:
Reaction–diffusion–advection
Reaction front
Microgravity
Convection
Radial Hele-Shaw
Parabolic flight

ABSTRACT

The dynamics of radial $A + B \rightarrow C$ reaction fronts can be affected by buoyancy-driven convection. Motivated by recent advances in reaction-diffusion–advection (RDA) systems theory, we investigated experimentally a radial $A + B \rightarrow C$ RDA system under modulated gravity, using a Hele-Shaw cell setup onboard a parabolic flight. We evaluated characteristic properties of the RDA models, such as the temporal evolution of the total amount of product C, the width and position of the reaction front and compared them with theoretical predictions. During increased gravity, we observed an increase in both the total amount of product C formed and the front width, compared to the corresponding normal-gravity experiments, caused by the stronger buoyancy-driven convection. Finally, we report on experiments performed entirely in absence of gravity, eliminating buoyancy-driven convection. Despite the short observation time, comparison with ground experiments showed the effect of buoyant convection on radial RDA fronts, enhancing mixing and increasing product generation.

* Corresponding author at: Institute of Fluid Dynamics, Helmholtz-Zentrum Dresden-Rossendorf, Bautzner Landstr. 400, 01328 Dresden, Germany.
E-mail address: g.stergiou@hzdr.de (Y. Stergiou).

https://doi.org/10.1016/j.ces.2022.117703
0009-2509/

1. Introduction

Reaction–Diffusion (RD) $A + B \rightarrow C$ fronts are generated when two initially separated chemical species, A and B, come into contact, mix diffusively and react to form a product, C, via the scheme $A + B \rightarrow C$. This leads to the formation of a sustained *chemical front*, i.e., a spatially localized region with a non-zero production rate. These RD fronts have been the focus of interest in an increasing number of studies since the work by Gálfi and Rácz in 1988. In a radial geometry (Fig. 1), a chemical front develops as a one-dimensional system (along the radial direction, r), when only A is present for $r < r_0$ and only B for $r > r_0$, where r_0 is the radius of initial contact. At $t = 0$ A and B come in contact triggering a reaction front where A and B are consumed and C is generated. Typical properties such as the concentration profiles of A, B and C, as well as the front width, W_C, are introduced in the schematic of Fig. 1a for $t > 0$.

Since the dynamics underlying these systems affect the spatiotemporal distribution of the product and the reaction yield, understanding the underlying physics and chemistry has long been of great scientific interest (Luther, 1906; Fisher, 1937; Kolmogorov et al., 1937). Detailed analytical (Gálfi and Rácz, 1988), experimental (Koo and Kopelman, 1991) and computational studies (Koo et al., 1990; Jiang and Ebner, 1990) have provided scaling laws for relevant reaction front variables.

RD dynamics have been used to describe a large variety of physical systems, e.g., epidemiology, as recently applied to the spread of COVID-19 (Mammeri, 2020), pattern formation in biology (Kondo and Miura, 2010), demographics and paleoanthropology (where human presence and expansion has been modelled through RD equations, accounting for environmental factors (Steele et al., 1998)), linguistics (as in the case of language death processes (Abrams and Strogatz, 2003)), population dynamics (Volpert and Petrovskii, 2009), ecology (Cosner, 2008), finance (Mastromatteo et al., 2014), digital image restoration (Zhao et al., 2018) and particle physics (Toussaint and Wilczek, 1983).

In numerous natural and technological applications, a reactant A is injected at a steady flow rate into a region initially occupied by a reactant B. These reaction–diffusion–advection (RDA) systems are of significantly increased complexity, especially when the advection flow field is not uniform. Consequently, reaction front systems under flow conditions have come into the focus of current research.

Applications of these $A + B \rightarrow C$ RDA systems are found in combustion (Williams, 1985), atmospheric chemistry (Seinfeld and Pandis, 2016), environmental systems (Abraham, 1998, De Wit, 2020), engineering geology (Malusis et al., 2003), and carbon capture and storage (CCS) (Luquot and Gouze, 2009). In chemical engineering and technology, RDA dynamics can play a role in microchip-oriented studies investigating certain types of microreactor technologies, e.g., under creeping laminar flow conditions (Helisaz et al., 2018; Balakotaiah et al., 1995). They further provide access to small-scale pattern formation in autocatalytic processes (Heidel et al., 1988). In the past, radial RDA setups were used to generate self-assembled precipitation structures (Hauser and Simoyi, 1994a; Hauser and Simoyi, 1994b; Balog et al., 2019), selective composition of the reaction product and thermodynamically locked crystals (Bohner et al., 2014).

Fig. 1b depicts a schematic overview of the RDA front in a planar geometry with central injection. A solution of reactant A is continuously fed into a solution of reactant B, which is initially present in the radial reactor, to form the product C. The flow velocity $\vec{U}(r)$ depends on the radial position r. Important variables to describe the reaction front are its radial distance from the inlet, r_f, and the front width, W_C. The full set of variables will be defined in detail later. For this radial geometry, scalings of the dynamics have been obtained by a one-dimensional approach that takes into account the gap-averaged radial flow velocity component, exploiting the radial symmetry of the system (Brau et al., 2017; Brau and De Wit, 2020). Experiments are typically carried out in Hele-Shaw (HS) cells, where the liquids are contained in a thin gap between two parallel plates, separated by a small, but finite gap height h. Hence, in practice, the assumption of a 1D problem is only valid if diffusive equilibration is fast enough so that the parameters can be considered as constant in the other geometrical directions.

When advection becomes significant, the effect of Taylor dispersion (Taylor, 1953; Aris, 1956) further enhances the mixing. In the fluid gap between the parallel plates of a Hele-Shaw cell, for the flow rates used, a parabolic velocity profile (Poiseuille flow) is formed. The higher flow velocity in the center of the gap deforms the reaction front, while diffusive transport takes place along the resulting small-scale concentration gradients. To account for Taylor dispersion, an approximate model for the non-uniform velocity field in the gap was included in Tóth et al. (2020). Later, an actual 2D numerical study of a reaction front in a radial Poiseuille flow was conducted (Comolli et al., 2021). Nevertheless, the full interaction of hydrodynamics and diffusive mixing can lead to more complex spatio-temporal concentration distributions in propagating concentration fronts (Perez et al., 2019; Guilbert et al., 2021), which can also depend on the initial conditions even in the long-time regime (Balakotaiah et al., 1995).

In addition, buoyancy-driven phenomena are known to affect the progression of reaction fronts (Horváth et al., 2014), even for a horizontally oriented Hele-Shaw cell with a small gap height (Rongy et al., 2008; Rongy et al., 2010; Eckert et al., 2012). Buoyant convection contributes to chemo-hydrodynamic pattern formation both in miscible (Almarcha et al., 2011; Klink et al., 2011; Köllner et al., 2014) and immiscible (Eckert et al., 2003; Schwarzenberger et al., 2012) reactive systems under gravity. Thus, additional convective mixing (Rongy et al., 2008; Rongy

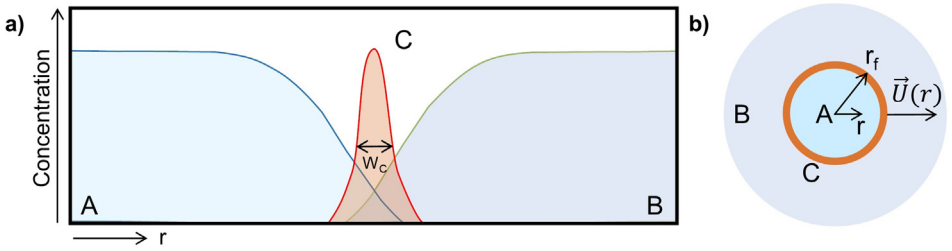

Fig. 1. (a) Schematic of a RD front in a qualitative concentration-distance view. The concentrations of the reactants (A, B) and product (C) are not to scale. (b) Schematic of a radial RDA front in top view. The injection flow results in a flow velocity $\vec{U}(r)$ that depends on the radial distance r. Characteristic measures such as the front width, W_C and outer radius, r_f are also shown.

et al., 2010; Eckert et al., 2012) can still be expected in a radial RDA system because of a slight density difference between the reactant and product solution, making a direct comparison to theory complicated or even impossible (Tóth et al., 2020; Brau et al., 2017; De Wit, 2020). Microgravity experiments enable us to distinguish between the contributions of buoyancy and deformation by the Poiseuille flow, making it possible to validate theoretical predictions on reactive chemical fronts. This strategy has also been employed for more fundamental diffusion-controlled experiments in microgravity conditions such as the Hard to Wet Surfaces (2016) experiment, investigating the dissolution and diffusion of solid tablets in liquids, and the experimental investigation of g-jitter effects on diffusion in binary mixtures, both on board the International Space Station (ISS); or the GRADFLEX experiment, on board the FOTON M3 spacecraft (Braibanti et al., 2019). Furthermore, the reaction–diffusion dynamics of a low Lewis number flame ball were studied under microgravity aboard the ISS (Ronney et al., 1998). Several other experiments also used microgravity to eliminate buoyancy-driven flows in order to investigate mass transfer phenomena such as Marangoni flows (Bába et al., 2018) or reaction–diffusion in immiscible systems (Eckert et al., 2012).

In addition to the decoupling of buoyancy-driven effects from other phenomena, experimenting on reduced or increased gravity gives us a first glimpse of how fundamental chemical processes might behave in the absence of gravity, revealing their potential use for *in situ* in-space manufacturing (Makaya et al., 2022). Microscale processes as in our study might provide solutions to problems that arise when transferring chemical technology to space (Hessel et al., 2020; Nijhuis et al., 2022). They further appear promising for process intensification in environments with reduced or increased gravity levels (Hessel et al., 2020).

In this work, we provide novel experimental insights into radial RDA dynamics for different levels of acceleration, in order to obtain quantitative data against which theoretical models can be tested. Due to the radially decaying front velocity, the influence of buoyancy strongly differs from the reaction–diffusion systems studied before. Hence, we conducted experiments using a well-known chemical reaction (Schönfeld et al., 2004; Tóth et al., 2020) in circular Hele-Shaw cells on board a parabolic flight (PF), i.e. under a sequence of alternating gravity levels (Section 2). We assessed the temporal evolution of the chemical fronts by examining characteristic front properties, such as the total amount of product formed (Section 3.1), and the position and overall width of the chemical fronts (Section 3.2). Comparison with the respective experiments on the ground allows us to evaluate the role of buoyant convection in the front dynamics, to relate the observed trends to the theoretical predictions, and to identify important requirements for future microgravity experiments on radial RDA fronts.

2. Chemical reaction, experimental setup and image analysis

As a model system for an $A + B \rightarrow C$ reaction, we employed the formation of the complex $FeSCN^{2+}$ (product C) from potassium thiocyanate KSCN (reactant A) and iron(III) nitrate $Fe(NO_3)_3$ (reactant B). This system was chosen for our radial injection study as the reaction front can be directly captured by absorption measurements: the product is intense in color in contrast to the colorless ractants (Tóth et al., 2020). Moreover, the fast reaction kinetics allows us to draw comparisons with existing theoretical RDA predictions, which assume instantaneous reaction (Brau et al., 2017; Comolli et al., 2019; Comolli et al., 2021). The experiments were performed in a quasi-two-dimensional planar geometry using the Hele-Shaw cell design described below.

The solutions were prepared from reagent-grade chemicals (Sigma–Aldrich) and deionized water. The HS cell was filled with a 0.03 mol L^{-1} $Fe(NO_3)_3$ aqueous solution, adjusted to acidic conditions (pH = 1) with HNO_3. Subsequently, a 0.03 mol L^{-1} KSCN solution was injected into the HS cell through the central inlet at a constant flow rate Q as in the work by Tóth et al. (2020). When the two solutions come in contact, the monocomplex $FeSCN^{2+}$ is predominantly produced at the solution concentrations used, following Eq. 1

$$SCN^- + Fe^{3+} \underset{k'}{\overset{k}{\rightleftharpoons}} FeSCN^{2+} \tag{1}$$

where $k \simeq 200$ L mol^{-1} s^{-1} and $k' \simeq 1.5$ s^{-1} (Below et al., 1958). Using the above, a fully mixed solution with equal volumes of reactant solutions results in a concentration of product C ($FeSCN^{2+}$) of $C_{fm} = 0.0075$ mol L^{-1}, as:

$$\frac{\left[FeSCN^{2+}\right]}{[SCN^-]\left[Fe^{3+}\right]} = \frac{C_{fm}}{\left(0.015\ \text{mol}\,L^{-1} - C_{fm}\right)^2} = \frac{k}{k'} \tag{2}$$

Table 1 lists the physical properties of the two reactant solutions and the resulting fully mixed product solution, as measured with an Anton Paar SVM 3001 pycnometer-viscosimeter (Anton Paar GmbH, Graz, Austria) at a temperature of 20 °C. The small viscosity differences combined with the low flow rates used prevent the emergence of viscous fingering during the experiment (De Wit, 2020).

The central component of our setup is the radial Hele-Shaw cell that is schematically depicted in Fig. 2a. The cell consisted of two parallel plates made of poly(methyl) methacrylate (PMMA). The overall observable radius (r_{max}) was 50 mm. The distance between the parallel plates could be set to three different gap height (h) values, namely: 0.2, 0.4, and 0.6 mm.

As shown in Fig. 2, the inlet port of the cell was attached through a threaded bore at the center of the bottom plate. To integrate the inlet tube, we used a custom-made connector system, consisting of a modified polytetrafluoroethylene (PTFE) connector plug (Bohlender GmbH, Grünsfeld, Germany) with an inner diameter of 1.0 mm. Four outlet ports with tubings were placed at the top of the reactor, through which the outflow was discharged into a waste container. To ensure that the flow was uniform, a large ring-shaped reservoir is machined into the upper PMMA plate outside the observable diameter. It serves as a buffer volume that prevents the generation of pressure gradients in the azimuthal direction. In this way, a preferential flow direction was avoided and the reaction front was kept radially symmetric within the HS cell. The gap-averaged (z-averaged) velocity U_r of the radial Poiseuille flow depends on the distance r from the injection point:

$$U_r(r) = \frac{Q}{2\pi h r} \tag{3}$$

In our HS cell design, the gap height h was set by a defined step in the rim of the top plate, which rests on the bottom plate (Fig. 2a). A

Table 1
Physical properties of reactant and product solutions (at 20 °C).

Solution	Density, kg m^{-3}	Viscosity, mPa s
A : KSCN, 0.03 mol L^{-1}	999.6 ± 0.1	0.97 ± 0.01
B : $Fe(NO_3)_3$, 0.03 mol L^{-1}, HNO_3 0.1 mol L^{-1}	1007.4 ± 0.1	1.08 ± 0.01
C : reacted mixture A and B, volume ratio 1:1	1003.0 ± 0.1	0.97 ± 0.01

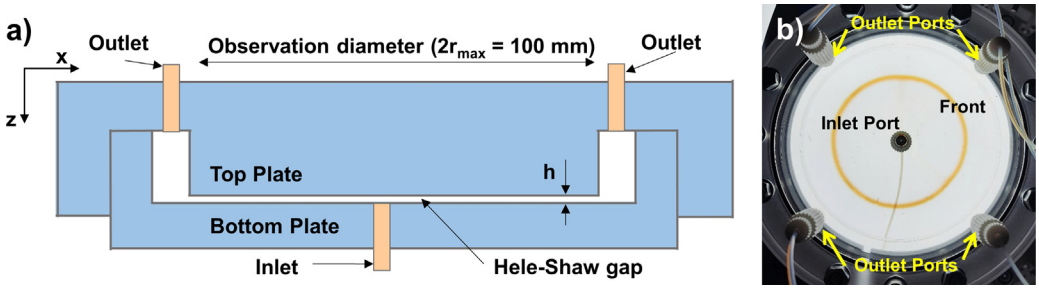

Fig. 2. Schematic vertical cross-section of the Hele-Shaw cell used in the experiments (a) and photograph of an experiment in progress showing the brown annular reaction front (top view) (b).

rubber O-ring was placed in a groove between the two PMMA plates to prevent leakage (not shown in the sketch for simplicity). The two HS plates were clamped together with 8 bolts and nuts that passed through holes near the edge of the two plates. Between these bores, 4 additional bores were installed, so that the HS cell could be fixed to the rest of the experimental setup.

The HS cells were mounted on a rotating circular aluminum disk supported by a central aluminum shaft (Fig. 3).

This experimental arrangement made it convenient to replace the HS cell occupying the optical path during the interval between the sequences of parabolas. A total of six HS cells could be integrated into the flight setup, but only one of them could be operated at a time. The plate of the rotating disk had six orifices where the cells were mounted so that the desired Hele-Shaw cell was optically accessible. The shaft of the carousel was fixed to an optical breadboard. The shaft was hollow and equipped with a lateral opening, such that the tubing for the reactant supply and the outflow of the product solutions could be accommodated inside.

The liquid injection system comprised two syringe pumps (PHD ULTRA™, Harvard Apparatus, Holliston, MA, USA) with two 50 mL gastight Hamilton 1050 syringes (Hamilton Company, Reno, NV, USA) and the liquid circuit. The syringe pumps offered a wide range of flow rates and operated in a stable way, i.e., no pulsation effect was observed in any of the gravity conditions visited during the parabolic flights. The selected injection flow rates were low enough to reduce hydrodynamic entrance phenomena that can cause intense reactant premixing (Stergiou et al., 2022). PTFE tubing with a nominal diameter of 0.8 mm and various valves (Bohlender GmbH, Grünsfeld, Germany) were used for the liquid circuit. The tube length between the inlet valve and the inlet port of each HS cell amounted to ≈ 175 mm. To activate the injection of the KSCN solution into one of the HS cells, the respective inlet valve was opened and the syringe pump set to run.

The reaction front was visualized by homogeneous illumination from below via a white light LED array with an integrated frosted glass plate (Smart Vision Lights, Norton Shores, MI, U.S.A.). The light emitted from the LED panel passes through the HS cell, where it is partially absorbed by the reaction product. It then reaches a JAI GO-5100 M, 2464 x 2056 px CMOS camera (JAI A/S, Copenhagen, Denmark) mounted above the HS cell. The camera objective (KOWA LM12SC Objective, Kowa Optimed Deutschland GmbH, Düsseldorf, Germany) was equipped with a Schneider BP 465–70 HT blue bandpass filter (Jos. Schneider Optische Werke GmbH, Bad Kreuznach, Germany). The blue filter significantly enhances

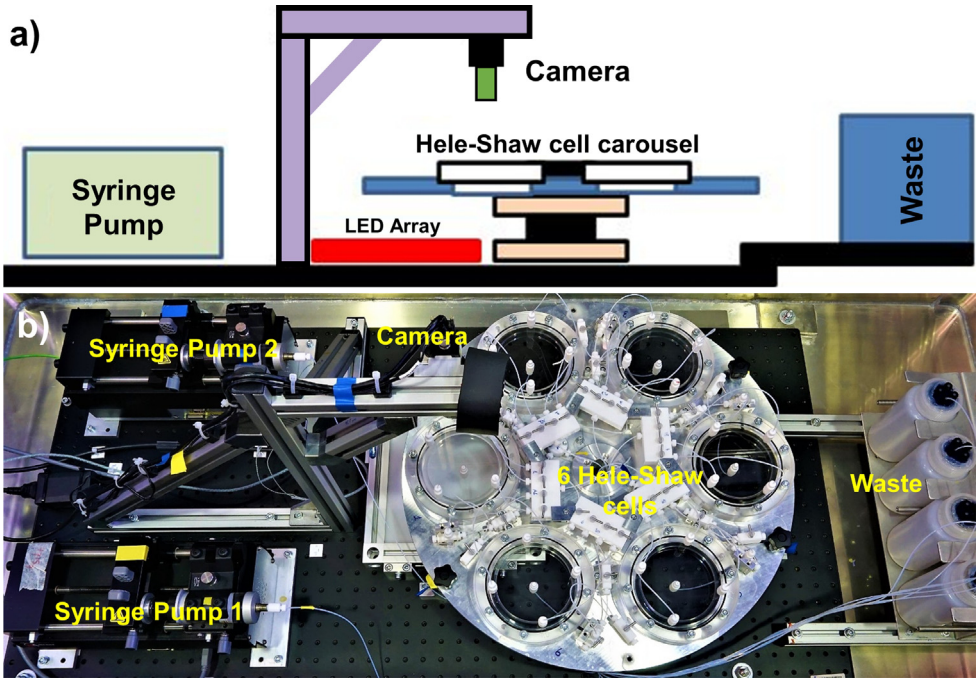

Fig. 3. Schematic diagram (a) and photograph (b) of the integrated experimental setup used for the parabolic flight experiments. The setup details are described in the text.

the contrast between the product and reactant solutions in the cases of small gap heights (the filter was used only for experiments with h = 0.2 or 0.4 mm). For all experiments, the objective was set to an f-stop value of 2.8 and a magnification value of 0.2. The camera was operated at a framerate of 10 Hz.

In addition, two temperature probes were integrated close to the HS cell of the running experiment in order to detect any spatial or temporal temperature gradients that might affect the front dynamics. The temperature difference between the two thermocouples did not exceed 1.0 K during the course of the experiment.

The whole setup was also equipped with an accelerometer (JoyWarrior56FR1, Code Mercenaries GmbH, Schönefeld, Germany) that was mounted near the carousel shaft. The accelerometer provided real-time acceleration values along all 3 axes (see Fig. 4).

The parabolic flight experiments were carried out on board a modified Airbus A310 aircraft (Air Zero G, Novespace, Bordeaux, France), during the 73rd ESA Parabolic Flight Campaign. To comply with the safety regulations of the A310 Zero-G aircraft, the experimental hardware was placed inside an aluminum container (750 mm x 1650 mm x 670 mm, Zarges GmbH, Weilheim, Germany).

During a typical parabola, shown in Fig. 4a, the aircraft initially starts ascending at a $\approx 50^{\circ}$ pitch angle with respect to the horizon using engine thrust and elevator control, while experiencing hypergravity. This means that the acceleration pointing down to the floor of the aircraft feels like approximately twice that of gravity. After a short transition phase, the microgravity phase starts, lasting around 22 s. This weightlessness feeling is achieved by reducing the motors' thrust and lowering the aircraft's pitch to maintain a net-zero lift configuration. During this phase, all the forces exerted on the aircraft roughly sum up to zero. Consequently, the aircraft is technically in freefall following a ballistic trajectory, with the low engine thrust compensating for the drag losses. The micro-G phase begins while the aircraft is still ascending and lasts for the entire top section of the parabola, until the aircraft reaches a downward pitch angle of about 40°. This is followed by an exit pull-out maneuver, necessary to remove the aircraft from a high-speed downwards motion and lead into a steady flight configuration in order to repeat the maneuver. The forces felt are again about twice as that of gravity, i.e., a hypergravity phase is experienced again.

Between the parabolic maneuvers a one-minute period of steady flight with normal gravity intervenes. The parabolic flight comprised a combination of 6 groups of 5 parabolic maneuvers. Each experiment was performed during a sequence of 5 parabolas, where one HS cell (with a constant gap height) was fed with reactant A solution at a constant Q in each case. During the sequence of parabolas, the HS cell was subjected to the different gravity regimes, that is, hyper-G ($\approx 1.8\ G$), zero-G ($\approx 10^{-2}\ G$) and 1-G. Here, $G = g/g_0$ denotes the normalized acceleration, where g is the instantaneously measured (i.e., apparent) acceleration and g_0 is the gravity acceleration on Earth, for which a value of 9.8 m s^{-2} is used. The frame of reference was set using the aircraft's principal axes; the z-axis is the yaw axis and the x-axis is the roll axis of the aircraft (Fig. 4a). This reference system coincides with the reference system applied in the experimental setup in Fig. 2. The typical acceleration values along the z- and x-axes of the aircraft are presented in Fig. 4b, in the course of 4 parabolas. The acceleration along the y-axis (the pitch axis of the aircraft) is of even lower magnitude than along the x-axis and was therefore excluded from the graph for clarity.

In parallel to the parabolic flight experiments, ground reference runs were performed with the flight hardware setup in an identical manner. Each experiment conducted in parabolic flights was repeated several times in laboratory conditions on ground with identical parameters (i.e., same h, Q combination) to ensure reproducibility.

Image processing. From the acquired images, the spatial and temporal concentration distribution of the product, $c(x,y,t)$ was obtained as in the work by Tóth et al. (2020). Here, x and y are the Cartesian coordinates in the HS cell. Time $t = 0$ was set when the front first appeared in the center of the HS cell (distinct color change in inner diameter of inlet plug), i.e., t is the time elapsed since the KSCN solution starts to be delivered to the HS cell. To determine the concentration distribution, the first step was to calculate the local relative gray value, $I(x,y,t)$, cf. Fig. 5c, from the local gray scale intensity, $I_c(x,y,t)$, and the reference intensity, $I_0(x,y)$, of the background image of the HS cell, containing only the $Fe(NO_3)_3$ solution:

$$I(x,y,t) = \frac{I_0(x,y) - I_c(x,y,t)}{I_0(x,y)} \tag{4}$$

The $I(x,y,t)$ value can then be directly assigned to a local concentration value $C(x,y,t)$ using previously obtained calibration curves. For calibration, the HS cell is filled with solutions with various, but constant product concentrations as described by Tóth et al. (2020). It should thus be noted that the determined concentration values are, per se, averaged over the total gap height

$$C(x,y,t) \equiv \frac{1}{h}\int_0^h C(x,y,z,t)\,dz \tag{5}$$

A distinct calibration curve was determined for each cell (gap height) and used in the subsequent analysis. In cells with narrow gap sizes (0.2 mm and 0.4 mm), a blue filter is used to enhance the optical contrast; this was also used during calibration. The calibration curves and their parameter values corresponding to each gap height are available as Supplementary Material. From the local

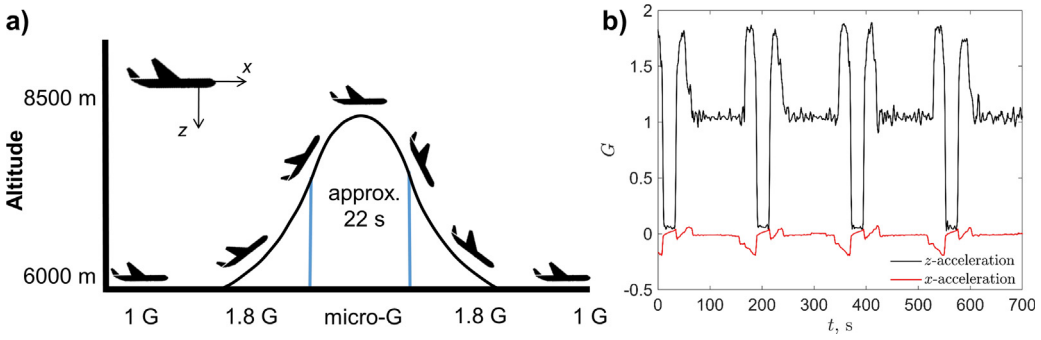

Fig. 4. A typical parabolic maneuver (a) and the two-axis acceleration values (for z-and x-axis, shown in black and red, respectively) acquired during a period of 4 parabolas (b). The frame of reference is also depicted with regards to the aircraft.

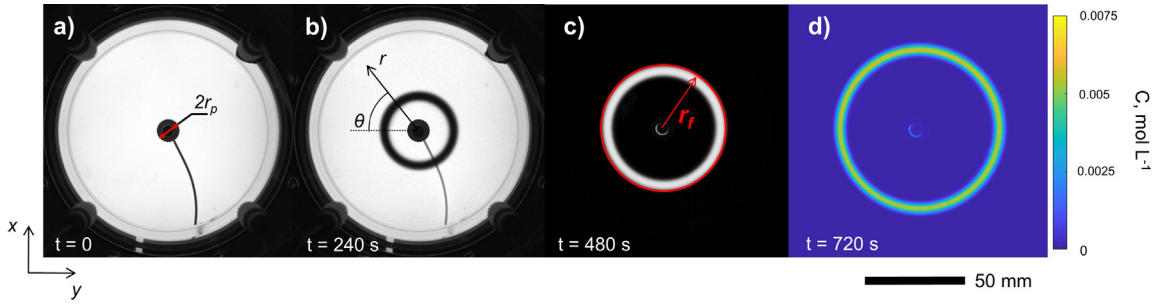

Fig. 5. Steps in the image processing procedure: raw image at t = 0 (a), raw image with a chemical front at t = 240 s (b), processed image with front tracking at t = 480 s, the front's outer limit, r_f, is highlighted (c), concentration distribution at t = 720 s (d).

concentration distribution, the total amount of product, n_C, present in the reactor can be calculated for each time, t, as:

$$n_C(t) = h \int C(x,y,t)\,dxdy \tag{6}$$

A normalized total amount of product can be introduced:

$$\overline{n}_C(t) = \frac{n_C(t) - n_{C,1}}{n_{C,fm}} \tag{7}$$

where $n_{C,1}$ is the total amount of product present after the reaction front detaches from the inlet plug radius, r_p. This value roughly corresponds to the amount of product that already enters the HS cell by the reaction in the inlet valve and tubing. Subtracting this baseline takes into account the fact that in the parabolic flight (PF) experiment, depending on the experimental conditions (i.e., acceleration conditions, manual valve handling between the parabola sequences), different quantities of product C might be present in the reactor at $t = 0$ due to premixing effects. The fully mixed amount of product $n_{C,fm}$ represents the product contained in the HS cell reactor if equal volumes of the reactant solutions were homogeneously mixed. It can be calculated as:

$$n_{C,fm} = \pi r_{max}^2 h C_{fm} \tag{8}$$

where C_{fm} corresponds to the molar concentration of the product in a fully mixed solution of equal reactant volumes, thus $C_{fm} = 0.0075$ mol L^{-1}.

Furthermore, the total production rate, $\dot{n}_C(t)$:

$$\dot{n}_C(t) = \frac{dn_C(t)}{dt} \tag{9}$$

refers to the production rate of C averaged over the entire HS cell volume. Hence, this time-dependent reaction rate is an indicator of the total reaction progress over time.

To describe the local front properties, a radial concentration profile, $C(r,t)$, was computed by averaging over the polar angle, θ (at equidistant angle intervals of $\Delta\theta = 2.4°$), on a cylindrical coordinate system. Here, the origin is located in the center of the circular front, as shown in Fig. 5b. Then, the time-dependent width of the product front, $W_C(t)$, can be calculated as the full-width at half-maximum (*FWHM*) of the $C(r,t)$ profile (cf. SI). The region occupied by the PTFE inlet plug is excluded from the image analysis, hence $r > r_p$ (Fig. 5a), as are all the pixels that are covered by the inlet tube. Additionally, to characterize the front progression, the leading edge radius of the reaction front, r_f, is tracked by a thresholding operation (Fig. 5c). All the image analysis described was carried out using MATLAB routines.

3. Results and discussion

3.1. Amount of reaction product

In Figs. 6 and 7, the product generation is presented for experiments in HS reactor cells with a gap height of 0.2 mm and 0.4 mm, respectively, for a duration of 500–700 s, meaning that several consecutive parabolas have an effect on the dynamics. The flow rate Q was constant throughout the experiment at 0.072 mL min^{-1} (0.2 mm gap, Fig. 6) and 0.144 mL min^{-1} (0.4 mm gap, Fig. 7). These

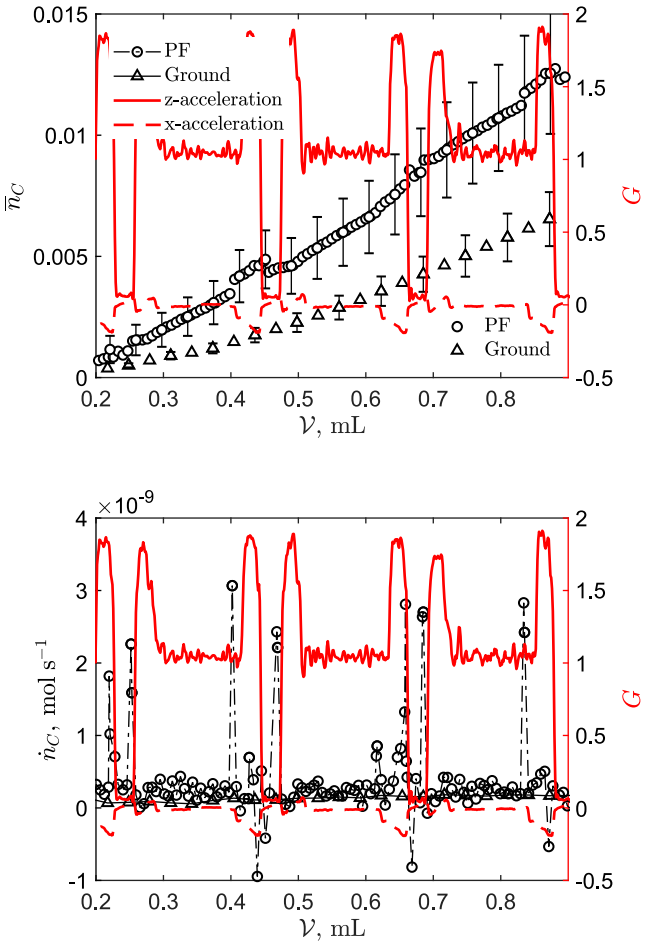

Fig. 6. Comparison of the normalized amount of product, $\overline{n}_C$ (top) and the total production rate, $\dot{n}_C$ (bottom) in experiments with h = 0.2 mm, Q = 0.072 mL min^{-1} on ground and during the PF. The corresponding acceleration values for the x- and z-axes are provided by the right axis.

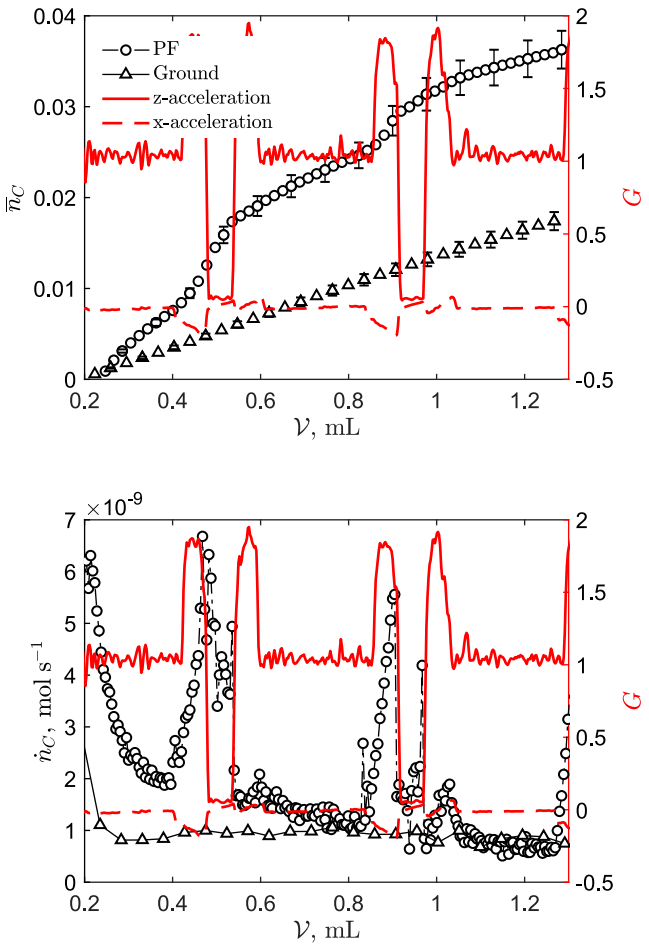

Fig. 7. Comparison of the normalized amount of product, $\overline{n}_C$ (top) and the total production rate, $\dot{n}_C$ (bottom) in experiments with h = 0.4 mm, Q = 0.144 mL min^{-1} on ground and during the PF. The corresponding acceleration values for the x- and z-axes are provided by the right axis.

values were selected to adapt the duration of the experiment to the time required to perform a sequence of 5 parabolas.

As a result, the two experiments share a common residence time, $\tau = \pi r_{max}^2 h Q^{-1}$ and a common average velocity distribution, $U_r(r)$. The same parameters were used in the respective ground reference runs in the laboratory. The results shown here from the ground reference experiments are an average over 3 repetition runs (cf. SM).

The normalized amount of product, $\overline{n}_C(t)$, and the product generation rate, $\dot{n}_C(t)$, are plotted against the injected volume, $\mathcal{V}$:

$$\mathcal{V} = Qt \tag{10}$$

where t is the time elapsed since the formation of the front in the HS cell. Note that $\mathcal{V}$ is directly proportional to time, since Q is constant in each experiment. This representation allows us to compare the required input of the KSCN reactant solution to generate the respective amount of product.

Figs. 6 and 7 show the evolution of the normalized total amount of product $\overline{n}_C$ (upper panel), the product generation rate $\dot{n}_C$ (lower panel), and the corresponding relative acceleration values G during the parabolic flight experiment (right-hand axis). At first sight, it is confirmed that the dynamics are clearly affected by the modulation of the gravitational acceleration. For both gap heights h of the HS cell, $\overline{n}_C$ is larger in the PF experiment. This can be attributed to the periodic change in acceleration (1-G, hyper-G and micro-G) along the z-axis and the additional slight modulations of the acceleration along the x-axis experienced by the fronts during the PF, and during the phase when the front enters the reactor (i.e., in Fig. 7, the front has already experienced a parabola at $\mathcal{V} = 0.2$ mL).

For the 0.4 mm gap height reactor (Fig. 7), the normalized amount of product formed $\overline{n}_C$ is considerably larger than for the 0.2 mm gap height reactor (Fig. 6). For example, at the same injected volume $\mathcal{V} = 0.8$ mL, in the 0.2 mm gap reactor $\overline{n}_C = 0.006$ on ground and $\overline{n}_C = 0.011$ during the PF, while in the 0.4 mm gap reactor, $\overline{n}_C = 0.010$ on ground and $\overline{n}_C = 0.024$ during the PF. The difference is even more significant considering that the corresponding time to inject the same $\mathcal{V}$ (which is the determining factor for diffusive mixing) is smaller in the 0.4 mm gap reactor. For this normalized product value (where the increase in the surface area between the reactant solutions is already taken into account), this can be attributed to the increased buoyant effects at a higher gap height, both on ground and during the PF. However, the contribution of the deformation by the Poiseuille flow also depends on the gap height. To compare the amount of product formed during the PF and on ground, it should further be noted that, at $\mathcal{V} = 0.8$ mL, the PF experiment in the 0.4 mm reactor was only subject to two acceleration modulation cycles (parabolas), while 3 parabolas were flown in the 0.2 mm gap reactor. Hence, the relative difference between the PF and ground experiments for the 0.4 mm gap is still comparable to the difference in the 0.2 mm case, despite the greater intensity of the buoyant phenomena present in the 0.4 mm gap experiment.

In the HS reactors with both gap heights, there is a jump to larger $\overline{n}_C$ values that coincides with the hyper-G phase of the parabolic maneuver. The underlying mixing effect induced by the gravity modulations is described in detail in the following. In the absence of density gradients, the front acquires and then conserves a parabolic shape (schematically sketched in Fig. 8a) attributed to the Poiseuille profile of the velocity field.

Under normal gravity conditions, the less dense KSCN solution (the densities of the solutions are presented in Table 1) flows preferentially towards the top of the HS gap, as depicted in Fig. 8b. This buoyant phenomenon is intensified either by increasing the gap height or by increasing the gravitational acceleration (Fig. 8c). In addition to the modulations of the z-axis acceleration, the nonzero x-axis acceleration during the hyper-G phase at the beginning of a parabola (Figs. 4b and 6, 7) interferes with the front dynamics. Although smaller in magnitude than the z-axis acceleration, the x-axis acceleration can likewise cause a local stretching of the front and hence enhance product generation. This effect can notably distort the annular shape of the front in the 0.4 mm reactor at the later stage of the experiment. At large t, the front has reached a larger radius, which leads to significantly lower velocities in the radial spreading of the front (cf. Eq. 3), and thus to a stronger impact of the slight horizontal acceleration. Therefore, only the first two parabolas are evaluated in the 0.4 mm gap experiment, where the circularity of the front is still preserved.

The error range for the amount of generated product in both Figs. 6 and 7 (upper panels) was estimated from the uncertainty in determining the calibration coefficients, and the manufacturing tolerance of the HS gap height (additional information on the uncertainty propagation estimation is provided as Supplementary Material). A further contribution to the experimental uncertainty during the PF is seen for the experiment with a 0.2 mm gap. During the acceleration modulations, specifically when changing from hyper-G to micro-G, a reduction in the amount of generated product was observed. This unphysical progression is probably due to the mechanical stresses to which the experimental setup is subjected during the gravity modulations. Especially during the hyper-G phase, the setup experiences twice the acceleration as on Earth, resulting in a possible bending and slight alteration of the optical path distances. Flight maneuver instabilities, motor vibrations

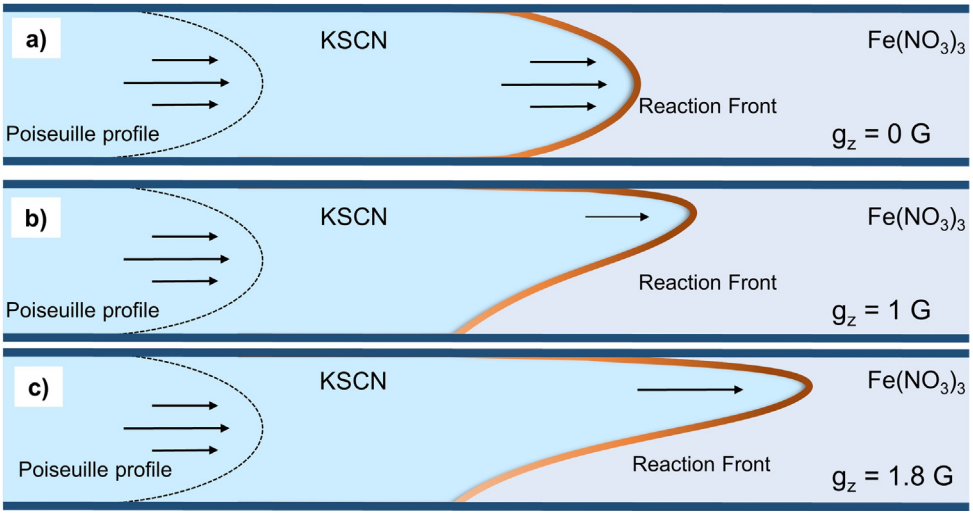

Fig. 8. Schematic representation of buoyant front deformation under three different gravitational levels: micro-G (a), 1 G (b) and 1.8 G (c) for the chemical front studied.

and local inhomogeneities in the atmosphere might be transferred to the setup to some extent despite the stabilizing profile construction. The calculation of the concentration distribution from the optical recordings of the reaction front is most sensitive to such disturbances in the case of the smallest gap size as the absolute concentration of the formed product is lowest with small gaps of this kind. Hence, the magnitude of this uncertainty was assessed based on the extent of the drop in the amount of generated product, and added to the given error range in both Figs. 6 and 7 (upper part).

In the lower panels of Figs. 6 and 7, the production rate $\dot{n}_C(t)$ is presented. For the 0.2 mm PF experiment, the production rate is scattered around the relatively constant ground values, but the average is at a higher level, compared to the respective ground experiment. This is mainly ascribed to the enhanced mixing by the acceleration modulations, as the front deformations during the comparatively shorter hyper-G phases carry on and continue to have an effect during the 1-G phases. In addition, the slight vibrations in the acceleration curves, that are generally seen in-flight, might also add to the enhanced mixing. The production rate highlights the dynamic situation during the parabolas. Instant spikes in the production rate are observed during the hyper-G phase at the beginning of a parabola, connected to the higher absolute x-axis acceleration values that act normal to the front.

The $\dot{n}_C(t)$ values for the 0.4 mm PF experiment appear much more robust than for the 0.2 mm case, as a result of the larger absolute amount of product present in the reactor compared to the experimental fluctuations. Negative production rates are absent throughout the whole experimental run, while spikes in production are observed during the hyper-G phases, as in the 0.2 mm gap experiment. This further suggests that the high production rates in the 0.2 mm gap are indeed a consequence of the enhanced mixing and are not primarily caused by the above-mentioned mechanical stresses acting on the setup.

The pronounced increase in $\dot{n}_C(t)$ during the hyper-G phases and, in particular, during the phases of nonzero x-axis acceleration is evident in the 0.4 mm experiment (values more than triple those of the corresponding ground cases are reached). In the normal gravity phases, the ground reference values are approached. Furthermore, it should be mentioned that the steep decline in high production rates, $\dot{n}_C(t)$ at the very early stage (i.e., for $0.2 < \mathcal{V} < 0.4$, Fig. 7) is caused by initial disturbances at the front, such as the effect of a residual premixed volume entering the cell and slowly spreading while the front progresses. This is most notable in the 0.4 mm case (both for on-ground and PF experiments) due to the wider reaction front. Additionally, when the front enters the reactor (i.e., at $\mathcal{V} < 0.2$ mL, not shown in Fig. 7 since the front is partially covered by the inlet plug), the gravity modulations might still affect the front dynamics; this is particularly noticeable at the very beginning of the $\dot{n}_C(t)$ curve.

For a qualitative comparison with the theoretical model (Brau et al., 2017; Tóth et al., 2020), the dimensional total amount of product $n_C(t)$ is plotted in Fig. 9 for the two different gap heights against the time elapsed, t. Fig. 9 focuses on the evolution in the later stage of the experiment, but before the front distortion caused by the x-axis acceleration becomes significant. The progression of the ground reference experiments at such a late stage suggests a linear dependence between the amount of product formed and time, i.e., $n_C \propto t$. Since this is in accordance with the analytical models (Brau et al., 2017; Tóth et al., 2020), the curves are approximated by a linear fit:

$$n_C(t) = St + p \tag{11}$$

where p is an offset factor. This approach yields an average production rate S (having units of mol s^{-1}), neglecting the discrete modulations in the PF experiment. The finding that $S_{PF} > S_{Ground}$ emphasizes how strongly the relatively short micro-G and hyper-G phases affect the production rate with respect to the long normal gravity intervals.

A similar fit (as in Eq. 11) is also suggested in studies that are based on a quasi-1D theory (Brau et al., 2017; Tóth et al., 2020). This approximation requires both diffusion to eliminate the concentration gradients across the gap and buoyancy effects to be absent. Indeed, the initially high density gradients will weaken in the later stages, and the product formation by diffusive mass transfer along the flow direction becomes more significant due to the decreasing velocities. However, the gravity-induced convective mixing that intensifies during the hyper-G phase is still notable. The higher S values during the PF compared to the ground case clearly indicate that this ideal situation has not yet been approached for either gap heights.

Comparison with a pure microgravity case. In some PF experiments with a large gap height (i.e., 0.6 mm and Q = 0.216 mL min^{-1}), the front was completely distorted towards the end of the experiment and the radial symmetry was lost, so that no consistent image analysis was possible (cf. SM). Therefore, a high flow

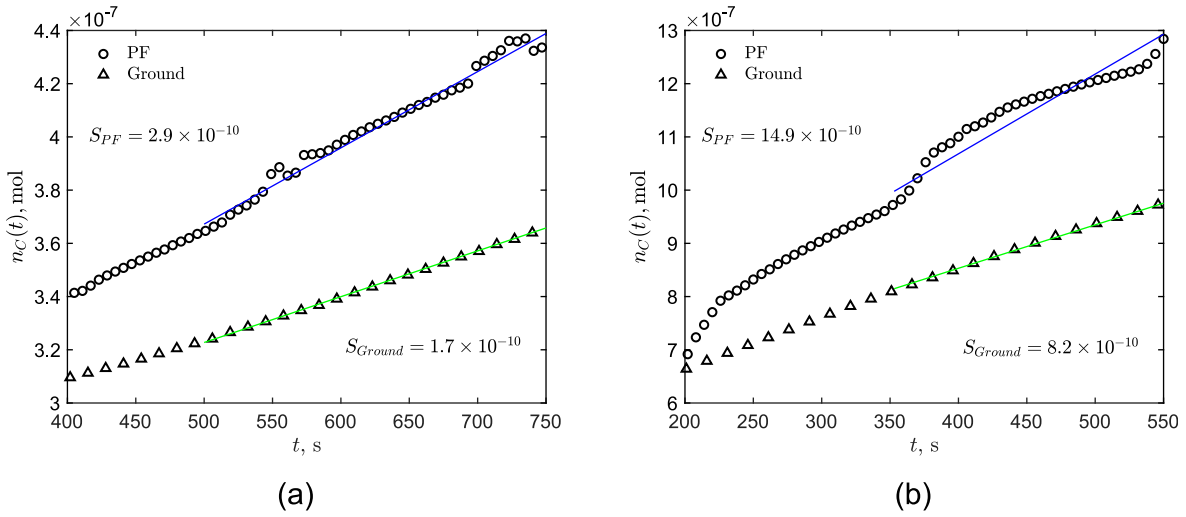

Fig. 9. Comparison between the dimensional total amount of product, $n_C(t)$ on ground and during the PF for two different experiments: h = 0.2 mm, Q = 0.072 mL min^{-1} (a) and h = 0.4 mm, Q = 0.144 mL min^{-1} (b). The S values have units of mol s^{-1}.

rate Q = 8.22 mL min^{-1} was used instead for the 0.6 mm cell, resulting in $\tau \approx 22$ s, which leads to injection occuring almost exclusively during a single micro-G period. Hence, this experiment serves as a comparison case which can provide initial insights into a radial RDA front without interfering buoyancy-driven effects. Here, the flow follows a parabolic profile and the reaction takes place at the stretched contact area between solutions *A* and *B*, as depicted in Fig. 8a. This "pure" microgravity experiment is presented in Fig. 10 together with the corresponding ground reference experiment.

Under these conditions, again, a significant deviation from the ground experiment is noticeable. In both cases, we observe a linear increase in the total amount of product formed. However, when the micro-G and the ground experiments are compared, the $n_C(t)$ in the constant 1-G ground experiments was always higher than in the PF experiments. It should be emphasized again that the acceleration conditions in this PF experiment are essentially different from the previous cases (zero-G in contrast to repeated gravity modulations) and hence had an opposite effect, i.e., a reduction in product formation. The remaining slight gravity modulations in the 0.6 mm cell at the very beginning and at the end of the experiment are negligibly small as they are not sufficient to exceed the product formation on Earth. Although the velocity of the radial flow is much higher than in the cases examined previously, buoyancy-driven phenomena play a major role in the ground reference case. The recorded reaction front images even show the emergence of a radially striped pattern towards the end of the experiment (cf. SM) which is a known buoyancy-driven instability in radial HS cells (Haudin et al., 2014; Pótári et al., 2019). The decreasing production rate $\dot{n}_C(t)$ in the later stages of the ground experiment is explained by the fact that the product starts leaving the observation window of the reactor. For example, at $\mathcal{V} = 3$ mL, the concentration C of the product at the rim of the reactor is approximately 5% of the maximum value in the radial concentration profile, i.e., a significant amount of product already flowed out. The faster progression of the reaction front towards the rim of the reactor in the ground experiment is also visible in the snapshots in the SM.

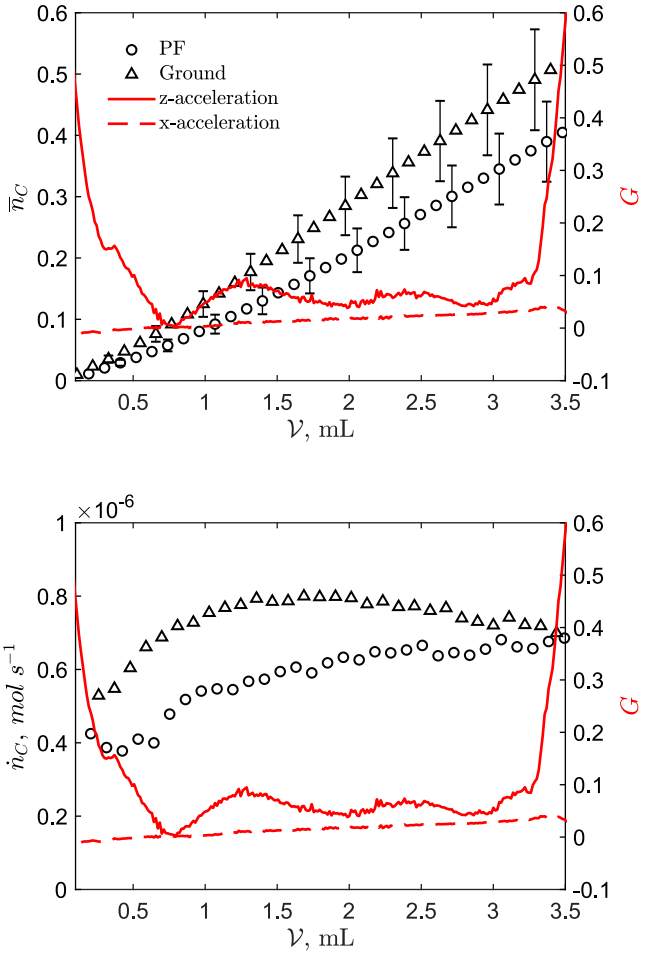

Fig. 10. Comparison of the normalized amount of product, $\overline{n}_C$ (top) and the total production rate, $\dot{n}_C$ (bottom) in experiments with h = 0.6 mm, Q = 8.22 mL min^{-1} on ground and during the PF. The corresponding acceleration values for the *x*- and *z*-axes are provided by the right axis.

3.2. Geometrical front properties

Since the PF experiment in the 0.2 mm gap height HS cell was subject to high experimental uncertainties as discussed before, the investigation of the geometrical front properties concentrates on the 0.4 mm gap height experiment. Two different measures for the front radius are analyzed and depicted in Fig. 11a for the ground and PF experiments. The r_C value is defined as the averaged

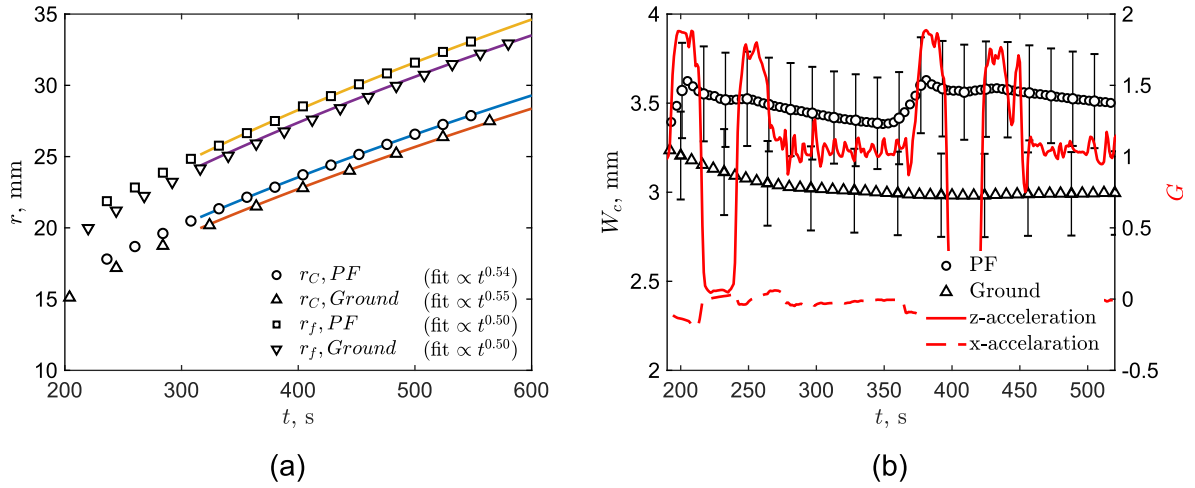

Fig. 11. Temporal progression of the front radii r_f and r_C (a) and of the front width W_C (acceleration values provided by the right axis) (b), on ground and during the PF for h = 0.4 mm, Q = 0.144 mL min^{-1}.

radial position where the concentration of the product C is maximum, and r_f is defined as the position of the outer rim of the reaction front (as shown in Fig. 5c).

Based on these definitions, the r_f value always exceeds the r_C value. Ideally, r_f is strictly dictated by the injection flow, and should scale with the square root of the injected volume, $\mathscr{V}$

$$r_f \propto \mathscr{V}^{0.5} \tag{12}$$

If the injection flow rate is constant, Eq. 12 implies that $r_f \propto t^{0.5}$. This is observed in Fig. 11a, in good agreement with the theoretical prediction. Likewise, the evolution of r_C is close to the $\propto t^{0.5}$ scaling proposed by Comolli et al. (2021). Indeed, we expect the gravity effects present in both the PF and the ground experiments to have a stronger impact on the position of the maximum C concentration (r_C), as this should coincide with the position of the highest density gradients. The amount of premixed volume entering the HS cell from the inlet tubing also might affect r_C more than r_f. In general, both front positions r_C and r_f are larger in the PF experiments, which can again be attributed to the enhanced mixing caused by the acceleration modulations along 2 different axes. However, no marked modulations in the front position curves are obtained due to the continuous spreading of the front caused by the injection flow.

Fig. 11b presents the temporal evolution of the front width. For the ground experiment, the front initially thins, then asymptotically approaches a constant value of $W_C \approx 3$ mm. The decrease at the beginning is ascribed to the non-ideal initial conditions, i.e., the spreading of the premixed volume as described above. The constant final width W_C qualitatively agrees with the progression predicted from theory (Comolli et al., 2021). In more detail, by utilizing an estimation for the governing time scale of the RDA dynamics (Comolli et al., 2021), we get a critical time, t_c:

$$t_c = \frac{hQ}{230\pi D^2} \tag{13}$$

where D is the diffusion coefficient, which we assumed to be equal for all the species. Its value of $D = 8.2 \times 10^{-10}$ m^2 s^{-1}, was estimated using experimental results (Tóth et al., 2020) for the same reaction system (Comolli et al., 2021).

For times shorter than t_c, the front dynamics are mainly governed by advective phenomena (e.g., deformation by the Poiseuille profile), while the front is dominated by diffusive mass transfer for times larger beyond t_c. For the reactor with a 0.4 mm gap height, using Eq. 13, it is estimated that $t_c \approx 2000$ s, which is significantly longer than the duration of the experiment. Thus, the front dynamics are still mainly controlled by advection by the injection flow, along with the effect of the premixed volume and buoyant convection. Only at much later stages would a continuous diffusive widening of the front (i.e., $W_C \propto t^{0.5}$) be expected from previous models (Comolli et al., 2019; Tóth et al., 2020; Comolli et al., 2021).

In the PF experiment, the effect of the gravity modulation on the z- and x-axes leads to the generation of more product and, as a consequence, to larger front widths. The W_C evolution correlates directly with the acceleration modulations, as the front width increases sharply during the hyper-G phase at the beginning of a parabola, while it decreases slowly during the subsequent micro-G and normal gravity phases (Fig. 11).

Comparison with a pure microgravity case. Lastly, Fig. 12 depicts the temporal progression of the reaction front width W_C and its radius r_f for the 0.6 mm HS cell and a flow rate of $Q = 8.22$ mL min^{-1} (i.e., the same experiment as in Fig. 10, with the whole injection taking place within one micro-G period). Due to the extremely large W_C, and the emergence of the radially striped pattern in the ground experiment, r_C is not considered and only the radius of the outer rim of the front r_f is evaluated in Fig. 12a for these experimental parameters. The wide reaction front also takes a considerable time to detach from the region covered by the inlet plug. Hence, a meaningful evaluation of W_C is only possible after some seconds in Fig. 12b.

While buoyancy effects strongly influence the evolution of W_C at low flow rates, the experiment under pure microgravity provides an initial quantitative approach for a comparison with the Taylor dispersion width, W_C^0, derived using the correlations proposed by Comolli et al. (2021):

$$W_C(t) = 1.23\sqrt{2Dt\left(1+\frac{3t_c}{4t}\right)} \tag{14}$$

For the early regime, $t \ll t_c$, this can be simplified as

$$W_C^0 \approx 1.23\sqrt{\frac{3}{2}Dt_c} \tag{15}$$

The underlying theory (Comolli et al., 2021) predicts that the value of W_C^0 will remain approximately constant until the front slowly transitions to the diffusive regime and can be better described by

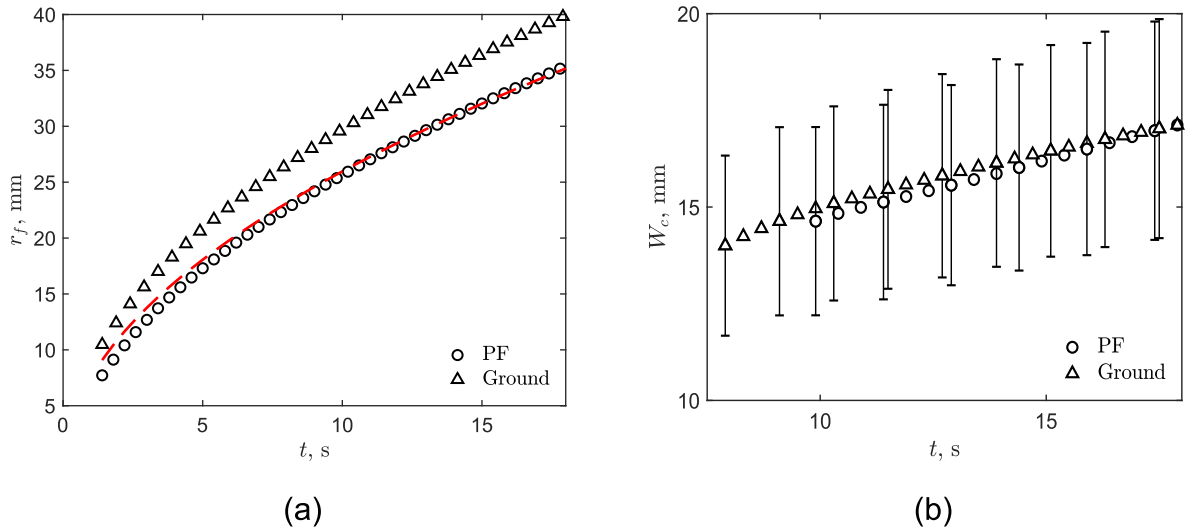

Fig. 12. Comparison of the temporal evolution of the front outer radius, r_f (a) and the front width, W_C (b) between a 1-G and micro-G experiment for h = 0.6 mm, Q = 8.22 mL min^{-1}. The dashed red line acts as a guide to the eye for a $\propto t^{0.5}$ scaling in (a).

Eq. 14, for $t \gtrsim t_c$. Using Eq. 13 for the case of $Q = 8.22$ mL min^{-1}, $h = 0.6$ mm, with the same diffusion coefficient as before, $D = 8.2 \times 10^{-10}$ m^2 s^{-1}, yields $t_c = 7 \times 10^5$ s. It is thus evident that in these high flow rate experiments, the front evolves long before the diffusion-controlled stage, when the front width is expected to follow a power-law (scaling with $t^{1/2}$) (Comolli et al., 2019; Comolli et al., 2021). The predicted value of the dispersive width, $W_C^0 \approx 18$ mm, approximately agrees with the experimentally observed W_C (see Fig. 12b).

In both experiments (ground and PF), the front width grows slightly towards the predicted W_C^0. However, the duration of the experiment is short, and the reactor has a limited horizontal extension in comparison to the wide front. Thus, the evolution is still in a transient initial phase, in contrast to the steady W_C^0 value that is expected in the case of a more extended reactor geometry. Certain variations in the initial conditions (volume of premixed solution, local product concentration distribution) add to the observed discrepancy from the estimate in Eq. 14 and can lead to unsteady product distributions before the quasi-steady Taylor dispersion regime is reached (Balakotaiah et al., 1995).

Despite the differences in the product formation, the evolution of the front width W_C obtained for the ground and PF experiment lie close together. However, comparing the evolution and magnitude of r_f in Fig. 12a reveals that the front progresses significantly faster on ground than in micro-G, including in the later stages. This can be attributed to a noticeable density current that causes the front tip to advance in the ground experiment. The density current is practically absent in the PF experiment. Moreover, the generation of the radially striped pattern might also affect the r_f dynamics towards the end of the ground experiment.

4. Conclusions

In this paper, we presented initial experiments on Reaction–Diffusion–Advection (RDA) fronts using radial Hele-Shaw cells under modulated gravity on board a parabolic flight. We *quantitatively* evaluated several RDA front parameters for a comprehensive characterization of the system dynamics and comparison with theoretical predictions. Although the density difference between the reactant solutions and the gap heights of the Hele-Shaw cells were small, the evolution of the front was still severely affected by the changing acceleration levels along the *z*- and *x*-axes. These modulations were directly reflected in the temporal evolution of product formation and of the front width. The resulting enhanced mixing under hyper-G conditions increased the total amount of product generated. Although the acceleration modulations in a horizontal direction were much lower in magnitude than the modulations in a vertical direction, they significantly contributed to the observed dynamics. In the short micro-G and longer 1-G phases, the observed peaks in production rate were further reduced. Moreover, an experiment performed entirely under micro-G conditions using a high flow rate confirmed the expected overall decrease in product formation in the absence of gravity. The comparison with the ground reference experiment proved that the micro-G conditions affect the front progression, even though the strong injection flow might be expected to dominate the dynamics at first sight. This experiment appears promising for a direct and quantitative comparison of our RDA model system with future theoretical studies.

Our parabolic flight experiments made it possible to test several *qualitative* and *quantitative* aspects of recent theoretical predictions. An approximately linear scaling of the total amount of generated product was found in the range of experimental parameters considered, with a larger slope accounting for the enhanced mixing under the influence of gravity. This simple scaling might be a convenient description even though it stems from the purely diffusive 1D theory, while our experiments are dominated by Taylor dispersion. Our experimental data reproduced the predicted front progression and a quantitative agreement for the front width was obtained for the high flow rate experiment.

However, our observations are also limited by certain experimental constraints. The selection of the ferric thiocyanate system allowed us to obtain data for fast reaction kinetics (i.e., high Damköhler numbers, which characterize the chemical reaction time scale in relation to the time scale of diffusive and convective mass transfer), approaching the theoretical predictions derived for instant reactions. Altering the mass transfer-to-reaction dynamics using a different kind of chemical system might reveal additional RDA dynamics regimes that are of great interest in technological applications, such as biological processes that involve macromolecules, polymerization and, even, particle precipitation processes for selective product generation. In the same vein,

employing more complex systems with higher acting density or viscosity gradients might be considered for future studies, as it would provide a wider view of the respective interactions and instabilities in radial RDA systems.

In addition, a longer and more stable micro-G environment throughout the whole injection time, such as in a sounding rocket flight (or in an ISS experiment), is required to avoid buoyancy effects and to cover different regimes. A longer experimental duration and continuous microgravity will lead to a complete absence of buoyancy-induced convective mixing and thus to lower total amounts of product. This would allow us to fully unravel the complex interactions in RDA systems. As a step towards this, our experiments have shown that a homogeneous and radially symmetric reaction front can be obtained, if horizontal acceleration is absent. Hence, our liquid-tight, robust Hele-Shaw cell design provides a good basis for future microgravity experiments in platforms offering extended microgravity periods.

Furthermore, the current study under modulated gravity provides a basis for transferring reaction–diffusion dynamics to space conditions. Our preliminary hands-on experience allows us to better estimate the performance of future extra-terrestrial chemical plants where processes involving reaction–diffusion–advection fronts will be significantly slowed down in environments with gravity levels lower than on Earth, in the absence of intense buoyant mixing, or, accelerated under hypergravity conditions. Thus, we hope that the results of this work will encourage future research involving chemical processes in space.

Declaration of Competing Interest

The authors declare that they have no known competing financial interests or personal relationships that could influence the work reported in this paper.

Acknowledgements

We thank Antonio Verga for his support during the parabolic flight campaign. Assistance regarding the parabolic flight preparations from Xuegeng Yang is gratefuly acknowledged. We would like to thank the Novespace team for their support before and during the parabolic flight campaign. We also thank the workshops of TU Dresden and HZDR for the setup construction, and Rolf Rostalski for kindly providing the photo for Fig. 3. Pauline Hagedorn is acknowledged for her help during the PF training. Discussions with the members of the ESA CHYPI-FLOWER Topical Team are greatly appreciated. This work was supported by the European Space Agency (ESA) and the German Aerospace Center (DLR) with funds provided by the Federal Ministry for Economic Affairs and Energy (BMWi) due to an enactment of the German Bundestag [Grant No. 50WM2061 (project ChemFront)]. A.C., F.B. and A.D. acknowledge the support of Prodex (Belgium) [Grant No. 4000129687]. A.C. acknowledges funding from the EU Horizon 2020 research and innovation programme under the Marie Skłodowska-Curie Action [Grant No. 801505]. G.S, P.P. and D.H. acknowledge the financial support of PRODEX [Grant No. 4000130733]. C.R and V. P were supported by the Centre Nationale d'Études Spatiales (CNES) [APRSDM 6273].

Appendix A. Supplementary material

Supplementary data associated with this article can be found, in the online version, at https://doi.org/10.1016/j.ces.2022.117703.

References

Abraham, E.R., 1998. The generation of plankton patchiness by turbulent stirring. Nature 391 (6667), 577–580. https://doi.org/10.1038/35361.

Abrams, D.M., Strogatz, S.H., 2003. Modelling the dynamics of language death. Nature 424 (6951). https://doi.org/10.1038/424900a. 900–900.

Almarcha, C., R'Honi, Y., De Decker, Y., Trevelyan, P.M.J., Eckert, K., De Wit, A., 2011. Convective mixing induced by acid-base reactions. J. Phys. Chem. B 115 (32), 9739–9744. https://doi.org/10.1021/jp202201e.

Aris, R., 1956. On the Dispersion of a Solute in a Fluid Flowing through a Tube, Proceedings of the Royal Society of London Series A 235 (1956) 67–77. https://doi.org/10.1098/rspa.1956.0065

Bába, P., Rongy, L., De Wit, A., Hauser, M.J.B., Tóth, Á., Horváth, D., 2018. Interaction of Pure Marangoni Convection with a Propagating Reactive Interface under Microgravity. Phys. Rev. Lett. 121 (2). 024501. https://doi.org/10.1103/PhysRevLett.121.024501.

Balakotaiah, V., Chang, H., Smith, F.T., 1995. Dispersion of chemical solutes in chromatographs and reactors. Philos. Trans. Royal Soc. London Series A: Phys. Eng. Sci. 351 (1695), 39–75. https://doi.org/10.1098/rsta.1995.0025.

Balog, E., Bittmann, K., Schwarzenberger, K., Eckert, K., De Wit, A., Schuszter, G., 2019. Influence of microscopic precipitate structures on macroscopic pattern formation in reactive flows in a confined geometry. PCCP 21 (6), 2910–2918. https://doi.org/10.1039/C8CP07693F.

Below, J.F., Connick, R.E., Coppel, C.P., 1958. Kinetics of the Formation of the Ferric Thiocyanate Complex. J. Am. Chem. Soc. 80 (12), 2961–2967. https://doi.org/10.1021/ja01545a015.

Bohner, B., Schuszter, G., Berkesi, O., Horváth, D., Tóth, Á., 2014. Self-organization of calcium oxalate by flow-driven precipitation. Chem. Commun. 50 (33), 4289–4291. https://doi.org/10.1039/C4CC00205A.

Braibanti, M., Artola, P.A., Baaske, P., Bataller, H., Bazile, J.P., Bou-Ali, M.M., Cannell, D.S., Carpineti, M., Cerbino, R., Croccolo, F., Diaz, J., Donev, A., Errarte, A., Ezquerro, J.M., Frutos-Pastor, A., Galand, Q., Galliero, G., Gaponenko, Y., García-Fernández, L., Gavaldá, J., Giavazzi, F., Giglio, M., Giraudet, C., Hoang, H., Kufner, E., Köhler, W., Lapeira, E., Laverón-Simavilla, A., Legros, J.C., Lizarraga, I., Lyubimova, T., Mazzoni, S., Melville, N., Mialdun, A., Minster, O., Montel, F., Molster, F.J., Ortiz de Zárate, J.M., Rodríguez, J., Rousseau, B., Ruiz, X., Ryzhkov, I. I., Schraml, M., Shevtsova, V., Takacs, C.J., Triller, T., Van Vaerenbergh, S., Vailati, A., Verga, A., Vermorel, R., Vesovic, V., Yasnou, V., Xu, S., Zapf, D., Zhang, K., 2019. European Space Agency experiments on thermodiffusion of fluid mixtures in space. Eur. Phys. J. E 42 (7), 86. https://doi.org/10.1140/epje/i2019-11849-0.

Brau, F., De Wit, A., 2020. Influence of rectilinear vs radial advection on the yield of A + B →C reaction fronts: A comparison. J. Chem. Phys. 152 (5), 054716. https://doi.org/10.1063/1.5135292.

Brau, F., Schuszter, G., De Wit, A., 2017. Flow Control of A + B →C Fronts by Radial Injection. Phys. Rev. Lett. 118 (13), 134101. https://doi.org/10.1103/PhysRevLett.118.134101.

Comolli, A., De Wit, A., Brau, F., 2019. Dynamics of A + B→C reaction fronts under radial advection in three dimensions. Phys. Rev. E 100 (5), 052213. https://doi.org/10.1103/PhysRevE.100.052213.

Comolli, A., De Wit, A., Brau, F., 2021. Dynamics of A+B →C reaction fronts under radial advection in a Poiseuille flow. Phys. Rev. E 104 (4), 044206. https://doi.org/10.1103/PhysRevE.104.044206.

Cosner, C., 2008. Reaction-Diffusion Equations and Ecological Modeling. In: Friedman, A. (Ed.), Tutorials in Mathematical Biosciences IV: Evolution and Ecology, Lecture Notes in Mathematics, Springer, Berlin, Heidelberg, 2008, pp. 77–115. https://doi.org/10.1007/978-3-540-74331-6_3.

De Wit, A., 2020. Chemo-Hydrodynamic Patterns and Instabilities. Annu. Rev. Fluid Mech. 52 (1), 531–555. https://doi.org/10.1146/annurev-fluid-010719-060349.

Eckert, K., Acker, M., Shi, Y., 2003. Chemical pattern formation driven by a neutralization reaction. I. Mechanism and basic features. Phys. Fluids 16 (2), 385–399. https://doi.org/10.1063/1.1636160.

Eckert, K., Rongy, L., De Wit, A., 2012. A + B→C reaction fronts in Hele-Shaw cells under modulated gravitational acceleration. Phys. Chem. Chem. Phys. 14 (20), 7337–7345. https://doi.org/10.1039/C2CP40132K.

Fisher, R.A., 1937. The Wave of Advance of Advantageous Genes. Annals of Eugenics 7 (4), 355–369. https://doi.org/10.1111/j.1469-1809.1937.tb02153.x.

Gálfi, L., Rácz, Z., 1988. Properties of the reaction front in an A + B →C type reaction-diffusion process. Phys. Rev. A 38 (6), 3151–3154. https://doi.org/10.1103/PhysRevA.38.3151.

Guilbert, E., Almarcha, C., Villermaux, E., 2021. Chemical reaction for mixing studies. Phys. Rev. Fluids 6 (11), 114501. https://doi.org/10.1103/PhysRevFluids.6.114501.

Hard to Wet Surfaces, 2016. https://gipoc.grc.nasa.gov/wp/other-iss/hard-wet-surfaces/.

Haudin, F., Riolfo, L.A., Knaepen, B., Homsy, G.M., De Wit, A., 2014. Experimental study of a buoyancy-driven instability of a miscible horizontal displacement in a Hele-Shaw cell. Phys. Fluids 26 (4), 044102. https://doi.org/10.1063/1.4870651.

Hauser, M.J.B., Simoyi, R.H., 1994. Inhomogeneous precipitation patterns in a chemical wave. Phys. Lett. A 191 (1), 31–38. https://doi.org/10.1016/0375-9601(94)90556-8.

Hauser, M.J.B., Simoyi, R.H., 1994. Inhomogeneous precipitation patterns in a chemical wave. Effect of thermocapillary convection. Chem. Phys. Lett. 227 (6), 593–600. https://doi.org/10.1016/0009-2614(94)00886-8.

Heidel, B., Knobler, C.M., Hilfer, R., Bruinsma, R., 1988. Pattern Formation at Liquid Interfaces. Phys. Rev. Lett. 60 (24), 2492–2495. https://doi.org/10.1103/PhysRevLett.60.2492.

Helisaz, H., Babaei, M., Sadeghi, A., 2018. Theoretical modeling of transient reaction–diffusion dynamics in electrokinetic Y-shaped microreactors. Chem. Eng. Sci. 191, 358–368. https://doi.org/10.1016/j.ces.2018.06.077.

Hessel, V., Sarafraz, M.M., Tran, N.N., 2020. The resource gateway: Microfluidics and requirements engineering for sustainable space systems. Chem. Eng. Sci. 225, 115774. https://doi.org/10.1016/j.ces.2020.115774.

Horváth, D., Budroni, M.A., Bába, P., Rongy, L., De Wit, A., Eckert, K., Hauser, M.J.B., Tóth, Á., 2014. Convective dynamics of traveling autocatalytic fronts in a modulated gravity field. Phys. Chem. Chem. Phys. 16 (47), 26279–26287. https://doi.org/10.1039/C4CP02480J.

Jiang, Z., Ebner, C., 1990. Simulation study of reaction fronts. Phys Rev A 42 (12), 7483–7486. https://doi.org/10.1103/physreva.42.7483.

Klink, O., Hanke, W., de Lima, V.M.F., 2011. Gravitational Influence on an Oscillating Chemical Reaction. Microgravity Sci. Technol. 23 (4), 403–408. https://doi.org/10.1007/s12217-011-9260-y.

Köllner, T., Rossi, M., Broer, F., Boeck, T., 2014. Chemical convection in the methylene-blue–glucose system: Optimal perturbations and three-dimensional simulations. Phys. Rev. E 90 (5), 053004. https://doi.org/10.1103/PhysRevE.90.053004.

Kolmogorov, A., Petrovskii, I., Piskunov, N., 1937. Study of a Diffusion Equation That Is Related to the Growth of a Quality of Matter and Its Application to a Biological Problem. Moscow University Mathematics Bulletin 1, 1–26.

Kondo, S., Miura, T., 2010. Reaction-Diffusion Model as a Framework for Understanding Biological Pattern Formation. Science 329 (5999), 1616–1620. https://doi.org/10.1126/science.1179047.

Koo, Y.E.L., Kopelman, R., 1991. Space-and time-resolved diffusion-limited binary reaction kinetics in capillaries: Experimental observation of segregation, anomalous exponents, and depletion zone. J Stat Phys 65 (5), 893–918. https://doi.org/10.1007/BF01049588.

Koo, Y.E., Li, L., Kopelman, R., 1990. Reaction Front Dynamics in Diffusion-Controlled Particle-Antiparticle Annihilation: Experiments and Simulations. Molecular Crystals and Liquid Crystals Incorporating Nonlinear Optics 183 (1), 187–192. https://doi.org/10.1080/15421409008047455.

Luquot, L., Gouze, P., 2009. Experimental determination of porosity and permeability changes induced by injection of CO_2 into carbonate rocks. Chem. Geol. 265 (1), 148–159. https://doi.org/10.1016/j.chemgeo.2009.03.028.

Luther, R., 1906. Räumliche Fortpflanzung chemischer Reaktionen. Zeitschrift für Elektrochemie und angewandte physikalische Chemie 12 (32), 596–600. https://doi.org/10.1002/bbpc.19060123208.

Makaya, A., Pambaguian, L., Ghidini, T., Rohr, T., Lafont, U., Meurisse, A. Towards out of earth manufacturing: Overview of the ESA materials and processes activities on manufacturing in space, CEAS Space. https://doi.org/10.1007/s12567-022-00428-1.

Malusis, M.A., Shackelford, C.D., Olsen, H.W., 2003. Flow and transport through clay membrane barriers. Eng. Geol. 70 (3), 235–248. https://doi.org/10.1016/S0013-7952(03)00092-9.

Mammeri, Y., 2020. A reaction-diffusion system to better comprehend the unlockdown: Application of SEIR-type model with diffusion to the spatial spread of COVID-19 in France. Computational and Mathematical Biophysics 8 (1), 102–113. https://doi.org/10.1515/cmb-2020-0104.

Mastromatteo, I., Tóth, B., Bouchaud, J.-P., 2014. Anomalous Impact in Reaction-Diffusion Financial Models. Phys. Rev. Lett. 113 (26), 268701. https://doi.org/10.1103/PhysRevLett.113.268701.

Nijhuis, J., Schmidt, S., Tran, N.N., Hessel, V., 2022. Microfluidics and Macrofluidics in Space: ISS-Proven Fluidic Transport and Handling Concepts, Frontiers in Space Technologies 2.

Perez, L.J., Hidalgo, J.J., Dentz, M., 2019. Upscaling of Mixing-Limited Bimolecular Chemical Reactions in Poiseuille Flow. Water Resour. Res. 55 (1), 249–269. https://doi.org/10.1029/2018WR022730.

Pótári, G., Tóth, Á., Horváth, D., 2019. Precipitation patterns driven by gravity current. Chaos 29 (7), 073117. https://doi.org/10.1063/1.5094491.

Rongy, L., Trevelyan, P.M.J., De Wit, A., 2008. Dynamics of A+B →C Reaction Fronts in the Presence of Buoyancy-Driven Convection. Phys. Rev. Lett. 101 (8), 084503. https://doi.org/10.1103/PhysRevLett.101.084503.

Rongy, L., Trevelyan, P.M.J., De Wit, A., 2010. Influence of buoyancy-driven convection on the dynamics of A+B→C reaction fronts in horizontal solution layers. Chem. Eng. Sci. 65 (7), 2382–2391. https://doi.org/10.1016/j.ces.2009.09.022.

Ronney, P.D., Wu, M.-S., Pearlman, H.G., Weiland, K.J., 1998. Experimental Study of Flame Balls in Space: Preliminary Results from STS-83. AIAA Journal 36 (8), 1361–1368. https://doi.org/10.2514/2.553.

Schönfeld, F., Hessel, V., Hofmann, C., 2004. An optimised split-and-recombine micro-mixer with uniform 'chaotic' mixing. Lab Chip 4 (1), 65–69. https://doi.org/10.1039/B310802C.

Schwarzenberger, K., Eckert, K., Odenbach, S., 2012. Relaxation oscillations between Marangoni cells and double diffusive fingers in a reactive liquid–liquid system. Chem. Eng. Sci. 68 (1), 530–540. https://doi.org/10.1016/j.ces.2011.10.033.

Seinfeld, J.H., Pandis, S.N., 2016. Atmospheric Chemistry and Physics: From Air Pollution to Climate Change. Wiley.

Steele, J., Adams, J., Sluckin, T., 1998. Modelling Paleoindian dispersals. World Archaeology 30 (2), 286–305. https://doi.org/10.1080/00438243.1998.9980411.

Stergiou, Y., Eckert, K., Schwarzenberger, K., 2022. Entrance effects in a radial Hele-Shaw cell: Numerical and experimental study. Chem. Eng. J. 428, 131146. https://doi.org/10.1016/j.cej.2021.131146.

Taylor, G.I., 1953. Dispersion of soluble matter in solvent flowing slowly through a tube. Proceedings of the Royal Society of London. Series A. Mathematical and Physical Sciences 219 (1137) (1953) 186–203. https://doi.org/10.1098/rspa.1953.0139.

Tóth, Á., Schuszter, G., Das, N.P., Lantos, E., Horváth, D., De Wit, A., Brau, F., 2020. Effects of radial injection and solution thickness on the dynamics of confined A + B →C chemical fronts. Phys. Chem. Chem. Phys. 22 (18), 10278–10285. https://doi.org/10.1039/C9CP06370F.

Toussaint, D., Wilczek, F., 1983. Particle–antiparticle annihilation in diffusive motion. J. Chem. Phys. 78 (5), 2642–2647. https://doi.org/10.1063/1.445022.

Volpert, V., Petrovskii, S., 2009. Reaction–diffusion waves in biology. Physics of Life Reviews 6 (4), 267–310. https://doi.org/10.1016/j.plrev.2009.10.002.

Williams, F., 1985. Combustion Theory: The Fundamental Theory of Chemically Reacting Flow Systems. 2nd Edition CRC Press, Boca Raton. https://doi.org/10.1201/9780429494055.

Zhao, X., Huang, K., Wang, X., Shi, M., Zhu, X., Gao, Q., Yu, Z., 2018. Reaction–diffusion equation based image restoration. Appl. Math. Comput. 338, 588–606. https://doi.org/10.1016/j.amc.2018.06.054.